Article

TEM Strata Inversion Imaging with IP Effect Based on Enhanced GCN by Extracting Long-Dependency Features

Ruiheng Li [1,2], Yi Di [1,3,*], Hao Tian [1,3,*] and Lu Gan [1]

1   School of Information Engineering, Hubei University of Economics, Wuhan 430205, China; liruiheng@cqu.edu.cn (R.L.); 20130263@email.hbue.edu.cn (L.G.)
2   State Key Laboratory of Power Transmission Equipment and System Security and New Technology, Chongqing University, Chongqing 400044, China
3   Hubei Internet Finance Information Engineering Technology Research Center, Hubei University of Economics, Wuhan 430205, China
*   Correspondence: diyi8710@hbue.edu.cn (Y.D.); th@hbue.edu.cn (H.T.); Tel.: +86-187-1716-0158 (Y.D.); +86-133-1718-2977 (H.T.)

Abstract: Utilizing neural network models to inverse time-domain electromagnetic signals enables rapid acquisition of electrical structures, a non-intrusive method widely applied in geological and environmental surveys. However, traditional multi-layer perceptron (MLP) feature extraction is limited, struggling with cases involving complex electrical media with induced polarization effects, thereby limiting the inversion model's predictive capacity. A graph-topology-based neural network model for strata electrical structure imaging with long-dependency feature extraction was proposed. We employ graph convolutional networks (GCN) for capturing non-Euclidean features like resistivity-thickness coupling and Long Short-Term Memory (LSTM) to capture long-dependency features. The LSTM compensates for GCN's constraints in capturing distant node relationships. Using case studies with 5-strata and 9-strata resistivity models containing induced polarization effects, compared to traditional MLP networks, the proposed model utilizing time-domain features and graph-topology-based electrical structure extraction significantly improves performance. The mean absolute error in inversion misfit is reduced from 10–20% to around 2–3%.

Keywords: transient electromagnetic inversion; strata electrical structure imaging; non-Euclidean features; long-dependency feature; graph convolutional networks (GCN); long short-term memory (LSTM)

1. Introduction

Using coils or long straight wires as signal transmitters generates time-domain-induced electromagnetic signals underground, enabling inference of the basic structure of subsurface electrical media [1–4]. This non-intrusive geophysical method, known as transient electromagnetic (TEM) detection, is extensively employed for subsurface imaging and exploration [5–7], particularly for low-resistivity target areas [8]. It finds broad applications in environmental monitoring [9,10], source exploration [11,12], and geological studies [13,14].

The process of inferring the electrical media structure from acquired time-domain electromagnetic induction signals is termed TEM inversion [15,16]. Strata media inversion based on single stations is commonly utilized for extensive geological surveys, often involving substantial data processing [13,17,18]. Traditional optimization methods like Newton's gradient descent are computationally inefficient for massive TEM survey data [15,19–23]. The rise of electromagnetic signal inversion using traditional multi-layer perceptron (MLP) addresses this challenge, with network models progressively deepening the extraction of electromagnetic signal features and geoelectric structural characteristics per layer [24–26]. However, a targeted feature extraction strategy is still lacking to enhance neural network performance [27].

When subsurface electrical media exhibit induced polarization (IP) effects [28,29], charges rearrange, impacting the trend of electromagnetic induction signals within specific

time windows [30–34]. This further exacerbates the nonlinearity of TEM inversion, posing a greater challenge to feature extraction in neural network inversion models.

For time-domain-induced electromagnetic signals, long short-term memory (LSTM) passes signals step by step via the time series, utilizing gate mechanisms to selectively retain time-domain signal features carrying crucial electrical media information [35,36]. This optimizes feature extraction from time-domain signals, enhancing the neural network model's predictive capability in electromagnetic signal inversion. However, concerning geoelectric structural features, containing attributes like resistivity and layer thickness, traditional Convolutional Neural Network (CNN) feature extraction, which excels in image processing, struggles to accommodate the non-Euclidean nature of resistivity-layer thickness pairs [25,37]. Given the success of topological graphs in handling irregular non-Euclidean data [38] incapable of satisfying translational invariance in tasks like node classification [39,40], graph classification [41], and link prediction [42], leveraging graph neural networks to further extract electrical structural features incorporating resistivity-layer thickness pairs is a viable option.

Given these considerations, we establish a neural network inversion model for time-domain-induced electromagnetic signals based on GCN's electrical media feature extraction. However, since each layer of GCN considers only first-order neighborhood information, it may struggle to capture complex relationships among distant nodes. To address this limitation, we use LSTM to capture long-dependency features [43,44], compensating for this shortcoming and enhancing the overall information aggregation capacity of the neural network model.

In the subsequent sections, we delve into the methodology in Section 2, reviewing the fundamental principles of TEM forward and inverse modeling. We elaborate on how the proposed neural network model employs LSTM to capture temporal dependency features from TEM-induced electromagnetic signals and uses GCN to capture spatial features of the geoelectric structure. Sections 3 and 4 present illustrative examples using five-strata and nine-strata geoelectric models, respectively. The discussions are presented in Section 5 and conclusions are presented in Section 6.

2. TEM Inversion with IP Effect

2.1. TEM Forward and Inversion

Consider a TEM device with a central loop, with the surface located outside the observation center point and surrounded by a coil with a radius of a. The center point is considered the observation point of the station and is used to receive electromagnetic induction signals. The z-axis is positive and negative below the ground [45]. Pass a current of amplitude I through the coil and immediately turn it off. The vertical magnetic field generated by the central observation station at the time of the cut-off time of 0, H_z, can be expressed as [15,24]:

$$H_z = \frac{Ia}{2} \int_0^\infty \left[e^{-u_0 z} + r_{TE} e^{u_0 z} \right] \frac{\lambda^2}{u_0} J_1(\lambda a) d\lambda, \tag{1}$$

where $z = 0$, u_0 can be approximated as λ, J_1 represents a first-order Bessel function, which is discretized using the Hankel transform for numerical integration. The surface reflection coefficient $r_{TE} = (\lambda - u'_1)/(\lambda + u'_1)$. u'_i is obtained by the layered recursive formula [46,47]:

$$u'_i = u_i \frac{u'_{i+1} + u_i \tanh(u_i h_i)}{u_i + u'_{i+1} \tanh(u_i h_i)} \quad u_i = \left(\lambda^2 - k_i^2 \right)^{1/2}, \tag{2}$$

here, N denotes the total stratum count of the geoelectric model, when $i = N$, $u'_N = u_N$. k is the wave number, $k_i = (-i\omega\mu\sigma)^{1/2}$, ω and σ denote the angular frequency and conductivity.

The Cole-Cole model is one of the mathematical models used to describe the polarization response of materials. It is widely employed in geophysics and electromagnetic exploration. Based on the complex dielectric function, the model depicts the relationship between electrical conductivity and permittivity of the geoelectric structure at various frequencies [48]. It encompasses parameters such as the polarization strength index, relax-

ation time, and initial phase. The Cole-Cole model is one of the expressions of this model and can be described as [15,49]:

$$\rho(\omega) = \rho\left(1 - m\left(1 - \frac{1}{1 + (i\omega\tau)^c}\right)\right), \tag{3}$$

where ω denotes angular frequency, τ represents the relaxation time associated with the planning mechanism. In the equivalent circuit of the rock unit, c denotes the frequency correlation coefficient. The coefficient m controls the reactive power performance.

The time-domain-induced vertical magnetic field $H_z(t)$ and induced electromotive force (EMF) ε can be transferred from frequency-domain induced magnetic field signals [3], and be obtained using the piecewise linear approximation method as follows [27,50]:

$$H_z(t) = -\frac{2}{\pi t^2}\sum_{i=0}^{N_t} \frac{\frac{\text{Im}[F(\omega_{i+1})]}{\omega_{i+1}} - \frac{\text{Im}[F(\omega_i)]}{\omega_i}}{\omega_{i+1} - \omega_i}[\cos(\omega_i t) - \cos(\omega_{i+1}t)], \tag{4}$$

$$\varepsilon(t) = -\frac{2\mu}{\pi t^2}\sum_{i=0}^{N_t} \frac{\text{Re}[F(\omega_{i+1})] - \text{Re}[F(\omega_i)]}{\omega_{i+1} - \omega_i}[\cos(\omega_i t) - \cos(\omega_{i+1}t)], \tag{5}$$

where N_t represents the number of time points, t denotes the time channel.

2.2. IP Effect on Inversion

When inversion is performed using the traditional gradient class method [15,51] when the initial geoelectric structure is a uniform half-space model, it is difficult to find the geoelectric structure that makes the TEM signal appear in the wrong direction (Figure 1a) during the inversion process, and the predicted geoelectric structure cannot be close to the preset structure (Figure 1b). The optimization process is stalled.
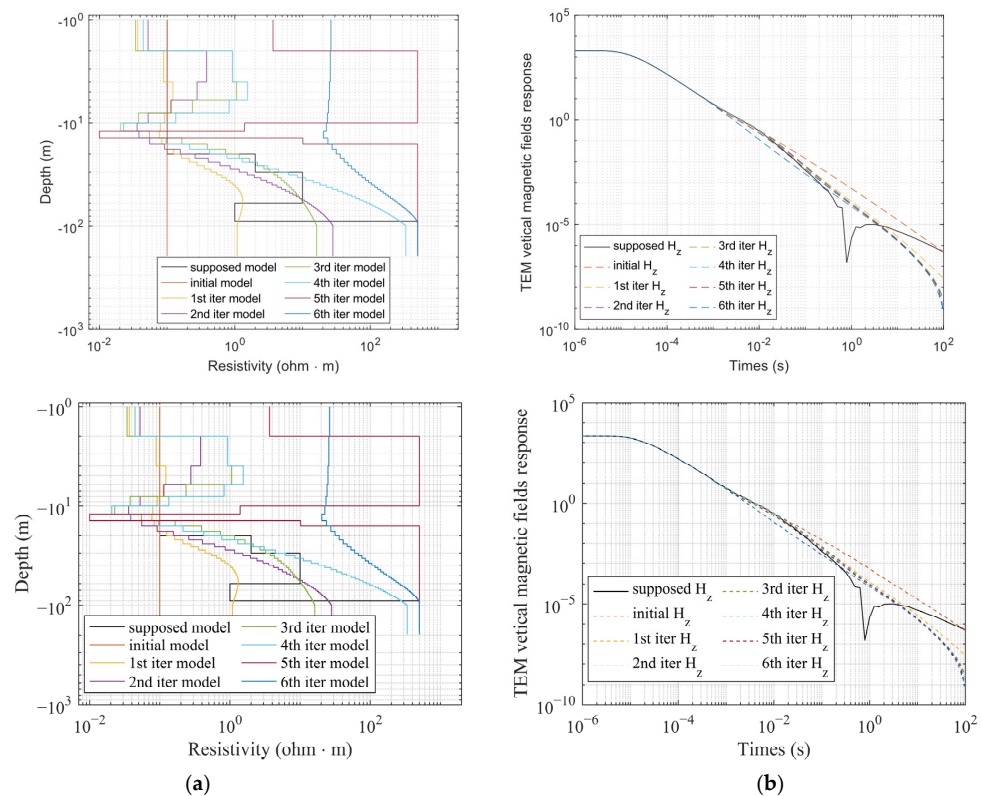

Figure 1. TEM inversion results considering IP-induced polarization effect. (**a**) represents the predicted TEM signal corresponding to the inversion iteration step, and (**b**) represents the predicted geoelectric structure corresponding to the inversion iteration step.

3. Our Networks Framework

3.1. Temporal Feature Capturing

The LSTM aims to tackle challenges such as gradient vanishing and the complexities associated with processing extended sequential data within recurrent neural networks. The structure of the LSTM model (Figure 2) involves an input layer, a recurrent hidden layer, and an output layer. Within the recurrent hidden layer, there exist components such as the forget gate (**F**), input gate (**I**), output gate (**O**), and memory cell (**C**). The memory cell (**C**) runs straight through the entire chain without any activation, preventing the gradients from vanishing when training the LSTM model using backpropagation [52].
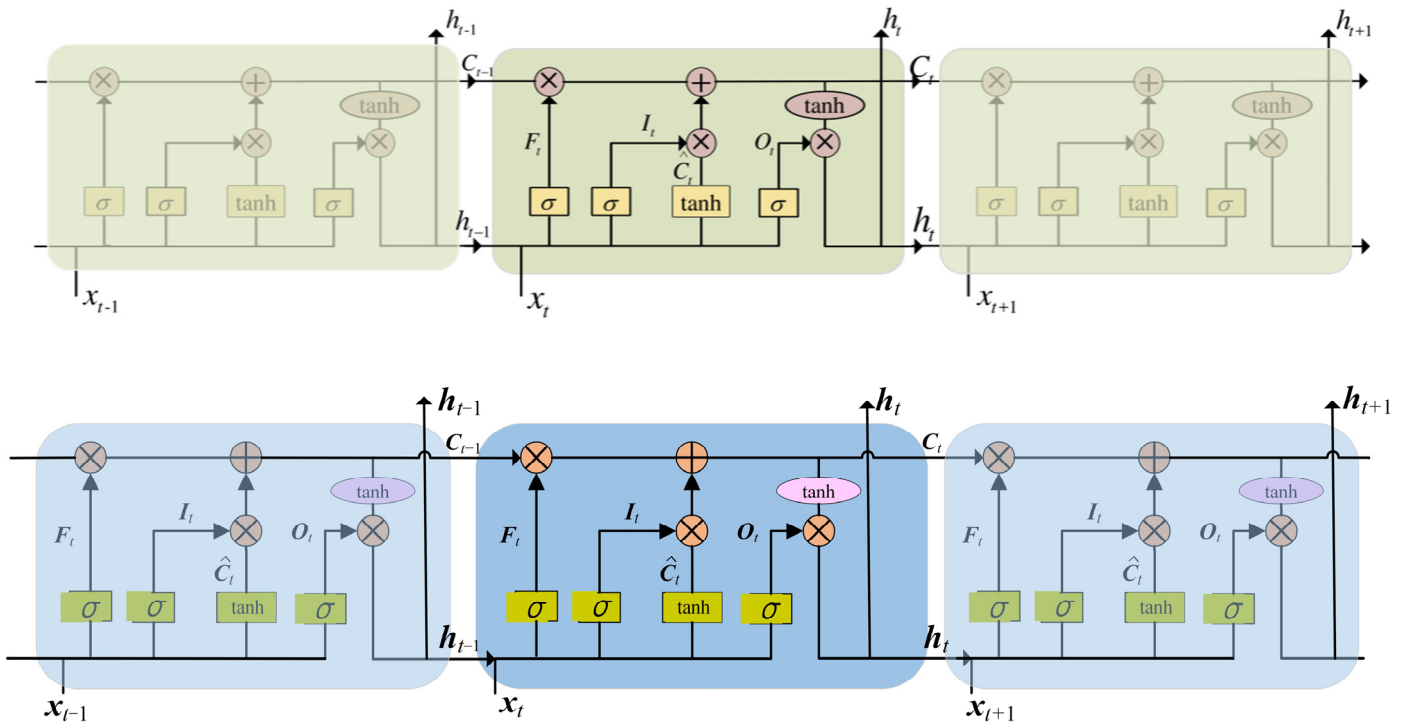

Figure 2. LSTM network architecture diagram.

LSTM model's gating update process is illustrated as follows:

Step 1: The forget gate, labeled as F_t, plays a crucial role in deciding which information should be retained within the memory cell C_{t-1} and what should be discarded [53]:

$$F_t = \sigma\Big(W_f \cdot [h_{t-1}, x_t] + b_f\Big), \tag{6}$$

Step 2: The input gate, denoted as I_t, is responsible for determining the new information that should be integrated into the memory cell [54,55]:

$$I_t = \sigma(W_i \cdot [h_{t-1}, x_t] + b_i), \tag{7}$$

$$\widehat{C}_t = \tanh(W_c \cdot [h_{t-1}, x_t] + b_c), \tag{8}$$

Step 3: Transitioning from the prior memory cell C_t to the updated memory cell involves [44,56]:

$$C_t = F_t \cdot C_{t-1} + I_t \cdot \widehat{C}_t, \tag{9}$$

Step 4: The role of the output gate, designated as O_t, is to regulate the quantity of information from the present memory cell C_t that should be directed towards the subsequent layer:

$$h_t = O_t \cdot \tanh(C_t), \tag{10}$$

where x_t symbolizes the input to the LSTM model during time step t, while h_{t-1} denotes the preceding time step's output from the recurrent hidden layer, and b denotes bias coefficients. W_f, W_i, W_o, W_c correspond to the weight matrices associated with F, I, O, and C, respectively.

3.2. Spatial Feature Capturing

We define the graph and feature matrix as follows:

Definition 1. *We utilize a graph $G = (V, E, A)$ to depict the topology of a geoelectric media structure, treating one stratum to be a distinct nodal point within this framework. Here, $V = \{v_1, v_2, \ldots, v_N\}$ signifies the collection of nodal points that corresponds to the electrical layers, and N signifies the count of nodal points. E denotes the edges within the graph. The adjacency matrix A captures the connectivity among electrical strata, denoted as $A \in R^{N \times N}$. This adjacency matrix solely consists of elements 0 and 1. An element within the matrix is assigned a value of 0 if there is no linkage between two layers; conversely, it takes on a value of 1 to signify a connection.*

Definition 2. *We utilize the electrical information within the geoelectric structure as attributes for the nodes in the network, denoted as $X \in R^{N \times P}$; here, P denotes the count of attribute features for every node, corresponding to the length of temporal series. Additionally, $X_t \in R^{N \times i}$ refers to the time-domain electromagnetic induction signals within each time window of instance i.*

Therefore, the challenge of TEM inversion for geoelectric structures m can be viewed as the acquisition of a supposing function f with the geoelectric strata topology G and the feature matrix X, as illustrated in Equation (1):

$$m = f(G; X), \tag{11}$$

The GCN model constructs a Fourier filter, allowing it to operate on the graph's nodes and capture spatial characteristics between them, specifically involving their first-order neighborhoods [57]. Multiple convolutional layers are then stacked to form the GCN model. Considering the adjacency matrix A, the propagation between layers in graph convolution is formulated as [58,59]:

$$H^{l+1} = sigmoid\left(\widehat{D}^{-1/2}\widehat{A}\widehat{D}^{-1/2}H^l W^l\right), \tag{12}$$

where $\widehat{D}$ denotes the degree matrix of $\widehat{A}$. H^l symbolizes the feature matrix for the l-th layer, while W^l pertains to the subsequent $(l + 1)$-th layer. The initial layer, denoted as H^0, corresponds to the feature matrix X. W^l stands as the weight matrix for the l-th layer.

In this study, a 2-layer GCN model is selected for capturing spatial correlations, formulated as follows [57]:

$$f(X, A) = sigmoid\left(\widehat{A}\text{ReLU}(\widehat{A}XW^0)W^1\right), \tag{13}$$

$$\widehat{A} = A + I \tag{14}$$

$\widehat{A}$ and $\widehat{D}$ are calculated using the following formulas:

$$\widehat{A}_{ij} = \begin{cases} 1, & i \neq j \\ 0, & i = j \end{cases}, \tag{15}$$

$$\widehat{\boldsymbol{D}}_{ij} = \begin{cases} \sum\limits_{j=1}^{N} \widehat{\boldsymbol{A}}_{ij}, & i = j \\ 0, & i \neq j \end{cases}, \tag{16}$$

where *A* represents the connection between each node. We choose a 2-layer GCN model, and Equation (12) is rewritten as [60,61]:

$$\boldsymbol{H}^2 = \text{sigmoid}\left[\boldsymbol{D}^{-1/2}\boldsymbol{A}\boldsymbol{D}^{-1/2}\text{sigmoid}\left(\widehat{\boldsymbol{D}}^{-1/2}\widehat{\boldsymbol{A}}\widehat{\boldsymbol{D}}^{-1/2}\boldsymbol{H}^1\boldsymbol{W}^1\right)\boldsymbol{W}^2\right], \tag{17}$$

We apply the GCN model to extract spatiotemporal characteristics from the time-domain-induced electromagnetic signals and the geoelectric strata structure. Illustrated in Figure 3, the model captures topological relationships between the central strata and its neighboring counterparts. It encodes both the road network topology and the geoelectric properties of the strata, thereby deriving spatial dependency relationships.
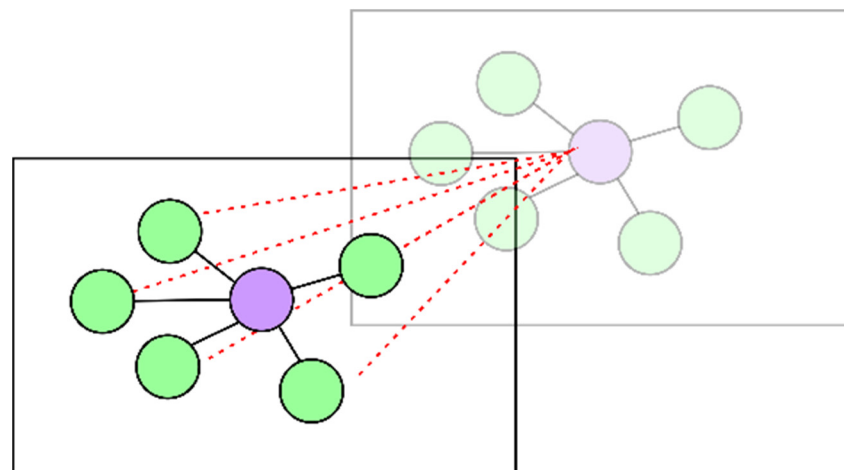

Figure 3. Assuming the central node (purple) represents the current geoelectric layer. The green nodes depict the connections to the current layer. We acquire spatial features by obtaining the topological relationships between the current geoelectric layer and its surrounding layers.

3.3. Network Inverse Frame

In TEM inversion, the induced time-domain electromagnetic response signals and the geoelectric structure exhibit complex non-Euclidean spatial patterns. The signal in each time-domain window is influenced by preceding time-domain window signals. Additionally, each geoelectric layer is interconnected with its adjacent layers. Our model comprises two primary components: a GCN and an LSTM network. We initially process the time-domain electromagnetic response signals of individual stations using the LSTM network to capture temporal features within the response signals (Figure 4). Subsequently, we employ the GCN to capture spatial correlations between different layers' topological structures in the geoelectric structure. The electrical features within each layer are treated as signals on the graph. Ultimately, we derive the outcomes of geoelectric structure from the induced TEM responses using fully connected layers.

By feeding the time-domain electromagnetic induction signals of each observation station into the LSTM network, the two types of TEM signals containing spatial information features, namely the induced magnetic field H_z signal and the induced EMF signal ε, are processed to extract temporal features. This results in features representing early, middle, and late stages. Subsequently, these features are input into the GCN to extract geoelectric spatial features. The function is expressed as follows:

$$Y_t = \sigma(\boldsymbol{W}_{He} \odot Y_{He} + \boldsymbol{W}_{Hm} \odot Y_{Hm} + \boldsymbol{W}_{Hl} \odot Y_{Hl} + \boldsymbol{W}_{ve} \odot Y_{ve} + \boldsymbol{W}_{vm} \odot Y_{vm} + \boldsymbol{W}_{vl} \odot Y_{vl}) \tag{18}$$

where Y_t represents the prediction target for the t-th time interval, $\odot$ denotes the element-wise multiplication, Y_e, Y_m, Y_l represent the feature outputs for the early, middle, and late stages, respectively, extracted using the LSTM network, W_e, W_m, W_l are learnable parameter tensors representing the degrees of influence from the early, middle, and late stages, respectively. The subscript H and the subscript v, respectively, indicate the magnetic field signal and the induced voltage signal.
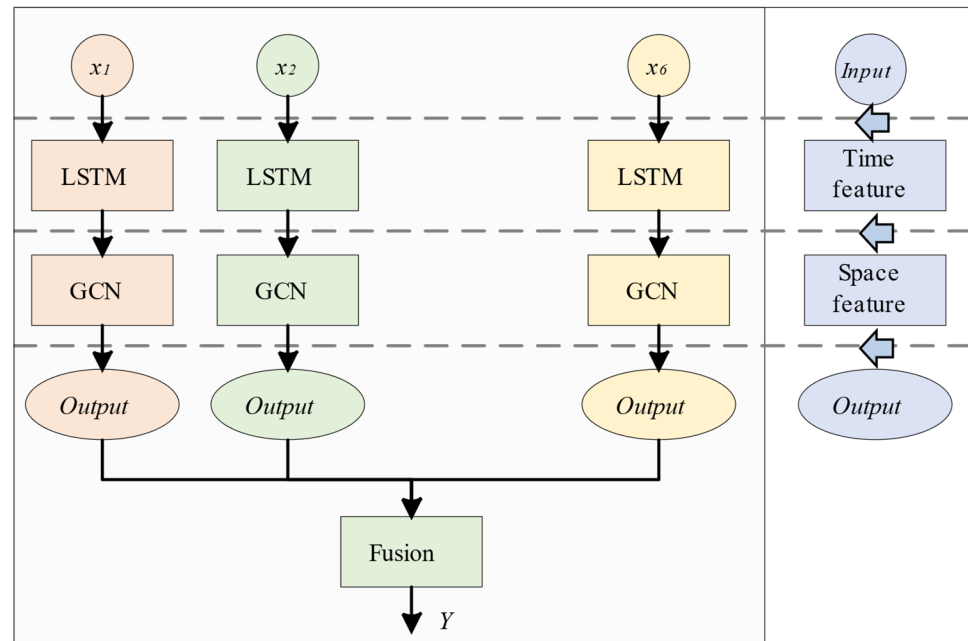

Figure 4. GCN-LSTM Model Framework.

3.4. Training

We established separate training samples for each layer based on different depths and used them to train different neural networks. In constructing the training samples, we randomly sampled the resistivity information for each layer within a range of $[1 \times 10^{-1}, 3.5 \times 10^3]$. For the layer thickness information in the geoelectric structure, we initially created a thickness sample library with values ranging from $[10, 1000]$ in a logarithmic scale with a base of $\log 2$. For simulating the excitation polarization effect, we considered the Cole-Cole model and randomly sampled the parameters m, τ, and c within the range of 0–1.

We divided the dataset containing 10 million samples into training and validation sets in an 8:2 ratio. We trained the proposed neural networks for 100 epochs, with the mean squared error as the objective loss function. The training process for the neural network suitable for a five-layer geoelectric model is shown in Figure 5. To determine the values of hyperparameters such as learning rate, network depth, and regularization rate, we also conducted a sensitivity analysis on these parameters.

When the learning rate is set to 0.01, both the training loss and validation loss decrease slowly during training, in contrast to the performance when the learning rate is 0.1. This indicates that with a learning rate of 0.01, the adjustment step size for the coefficients of each neuron is too small, resulting in inefficient training of the neural network.

Additionally, we compared the training performance of the neural network with different network depths, specifically 5, 10, and 15 layers. Regardless of whether the learning rate is 0.01 or 0.1, deeper networks result in smaller fitting errors for the neural network. The performance of the proposed network model on the training and validation datasets is summarized in the Table 1.
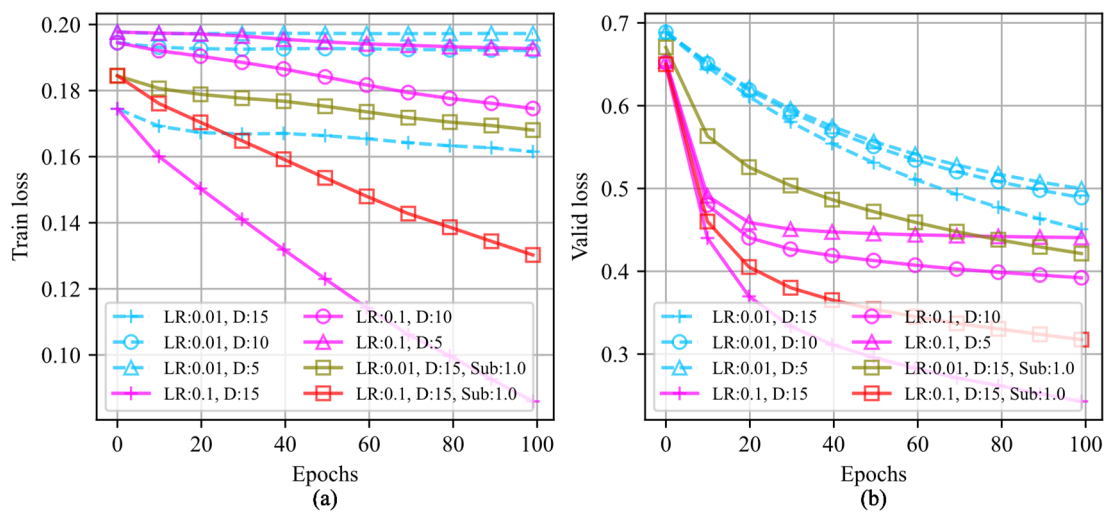
Figure 5. Training processes of the proposed neural networks correspond to different learning rates, network depths, and regularization rates. (**a**) represents the training loss decay; (**b**) represents the loss decay of valid dataset.

Table 1. Performance of the dataset under different neural network architectures.

	The Stack Depth			Loss	
				Train	Valid
GCN + LSTM	15	10	5	0.08	0.22
GCN	9	6	3	0.12	1.86
LSTM	6	4	2	12.94	3.17
MLP	15	10	5	0.16	2.04

4. Numerical Models

4.1. Model 1

To validate the precision of the GCN network model proposed in this study for transient electromagnetic inversion, we designed the multi-layer geoelectric simulation models and compared the inversion prediction capabilities of different neural network models based on TEM responses. Model 1 is set as a 5-strata geoelectric structure with a total of 9 predictive parameters.

In the setup, the TEM excitation-reception device uses a central loop and a circular loop with 20 m radius. A step turn-off current with an amplitude of 1 A is in the loop. The moment of current interruption is considered as time 0 s. The vertical component of the time-domain electromagnetic response signal is received starting from the observation station. The input signals to the neural network model are the induced magnetic field H_z and the induced EMF ε.

In the five-strata geoelectric model (Figure 6a), the resistivity of each layer is 50, 300, 100, 500, and 200 $\Omega \cdot$m, respectively. The thicknesses of the first four layers are 200, 250, 300, and 500 m, respectively. The bottom layer is considered an infinitely extending uniform space with infinite thickness. The third and fourth layers among the five layers are complex resistivity layers exhibiting IP effects. The Cole-Cole model represents the electrical structure of these two layers, and their frequency correlation coefficients are both set to 0.3.
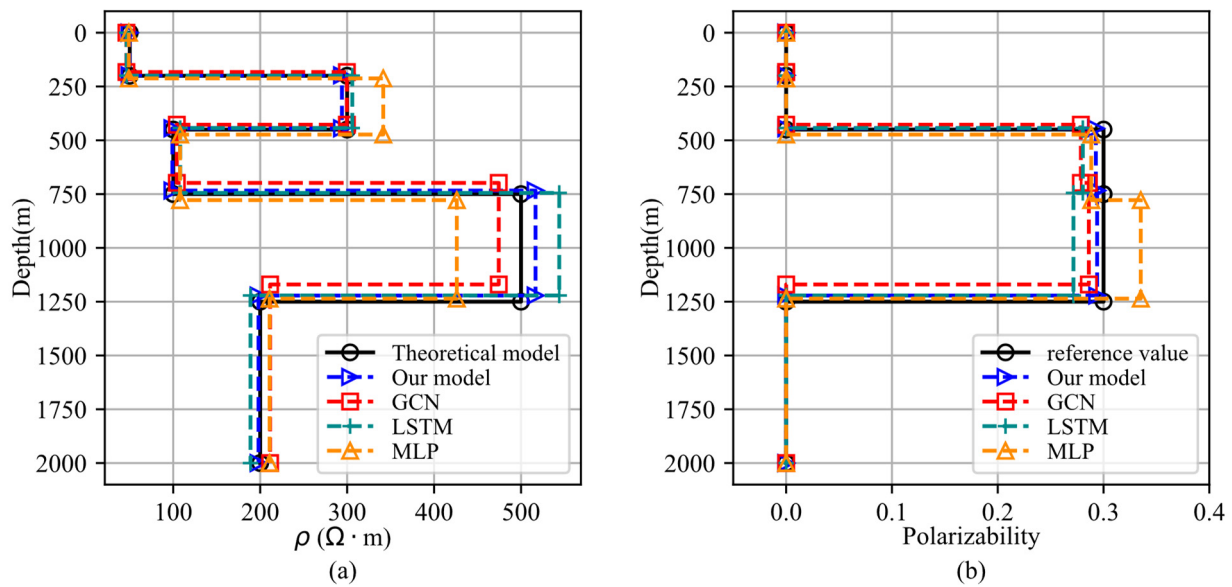
Figure 6. The predictions of different neural network models for the five-strata geoelectric structure based on TEM responses. (**a**) represents the depth-resistivity relationship chart for the assumed and predicted five-strata geoelectric structures. (**b**) represents the depth-IP (Induced Polarization) parameter relationship chart for the assumed and predicted five-strata geoelectric structures.

From the perspective of predicted geoelectric structure (Figure 6a), all four neural network models accurately predict the ρ and thickness h of the 1-st stratum. However, significant misfits are shown in the predictive resistivity of the 2nd layer, with MLP exhibiting the largest deviation among the methods. This deviation is further magnified in the prediction of the fourth layer's resistivity. The deviations follow a pattern of MLP having the highest, GCN and LSTM falling in the middle, and the proposed model has the smallest deviation.

Examining the accuracy of predicted polarization parameters for the third and fourth layers of this geoelectric model (Figure 6b), various methods exhibit relatively accurate restoration of the IP parameters for the third layer, while the accuracy drops for the fourth layer's IP parameters. In the prediction of the fourth layer's IP parameters, MLP performs the poorest, LSTM shows slight improvement, and the two GCN-based models achieve the highest accuracy in IP parameter prediction. The detailed predictions of the five-strata geoelectric model parameters by the four network models are represented in Table 2.

The accuracy of parameter predictions for the geoelectric model by different neural networks ranks from high to low as follows: our proposed model, GCN, LSTM, and MLP (Figure 7a). The inaccuracies in the geoelectric structure primarily concentrate on high-resistance layers, specifically layers with resistivities of 300 Ω·m and 500 Ω·m. In layers containing induced polarization effects, the accuracy of predicting the third-layer IP parameters generally surpasses that of predicting the fourth-layer IP parameters.

To comprehensively assess the prediction misfits of various network models, we conducted a comparative analysis of accuracy for the predicted geoelectric models' corresponding TEM responses as well (Figure 7c,d). The induced magnetic field misfits analysis reveals that the proposed method's prediction accuracy exhibits a substantial increase in two orders of magnitude in comparison to other methods, reducing the fitting discrepancy from 1×10^{-1} to 1×10^{-3}. The advantage of the proposed method, not manifested in the magnetic field misfits, becomes apparent in the comparison of EMF misfit (Figure 7d) prior to 1×10^{-8} s. Throughout the prediction process, the comparison of mean absolute percentage errors (MAPE) and root mean square errors (RMSE) for predicted resistivity, thickness, IP parameters, induced magnetic field, and induced EMF using different network models is presented in Table 3.

Table 2. Comparative details of four network models' predictions for the five-strata geoelectric model parameters.

	rho_1	rho_2	rho_3	rho_4	rho_5
Synthetic	50	300	100	500	200
GCN + LSTM	49.72	294.01	99.01	516.67	198.07
GCN	46.19	299.70	104.13	474.36	211.40
LSTM	46.39	305.93	108.02	543.94	188.85
MLP	48.96	341.54	107.87	426.10	210.80
	h_1	h_2	h_3	h_4	-
Synthetic	200	250	300	500	
GCN + LSTM	197.80	246.51	289.21	488.01	
GCN	182.96	244.69	270.20	472.07	
LSTM	199.31	243.80	301.43	476.49	
MLP	212.36	260.88	304.71	457.72	
	c_1	c_2	c_3	c_4	c_5
Synthetic	-	-	0.3	0.3	-
GCN + LSTM	-	-	0.293	0.294	-
GCN	-	-	0.279	0.286	-
LSTM	-	-	0.280	0.272	-
MLP	-	-	0.288	0.335	-

Note: rho_i, h_i, c_i represent the resistivity, thickness, and Cole-Cole model frequency correction coefficient of the *i*-th layer, respectively.
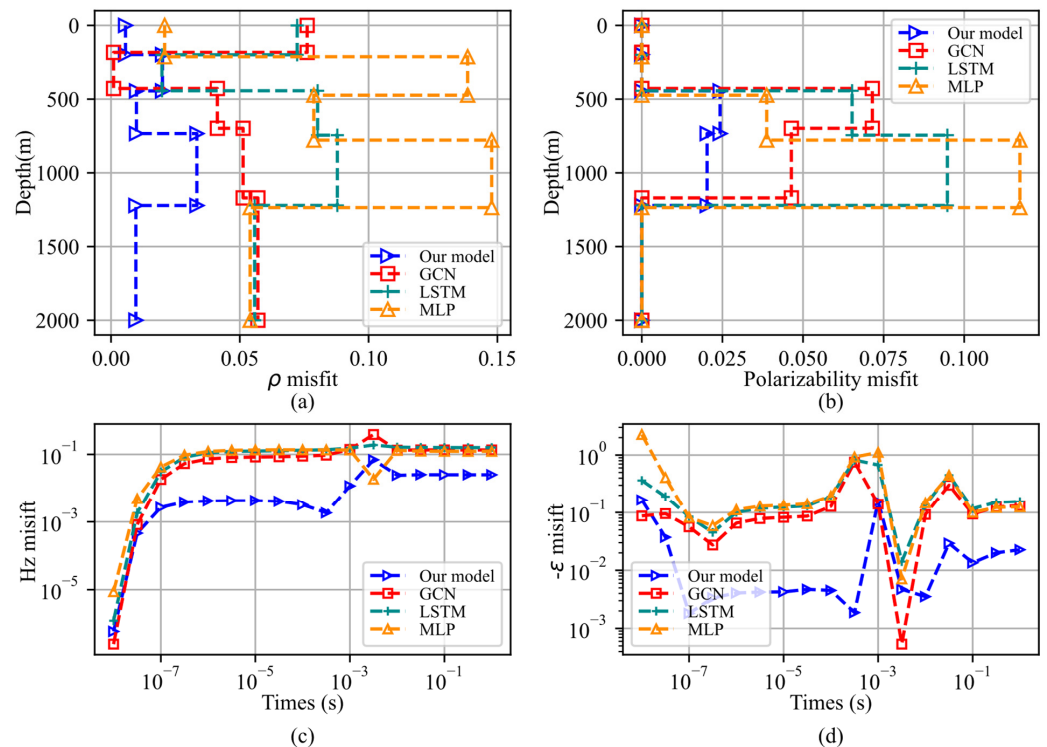

Figure 7. Misfit analysis of predicting the five-strata geoelectric structure using different neural network models based on TEM responses. (**a**) Depth and resistivity misfits of the predicted five-strata geoelectric structure, (**b**) Depth and IP parameter misfits of the predicted five-layer geoelectric structure, (**c**) Induced magnetic field misfits in the predicted TEM responses, (**d**) Induced EMF misfits in the predicted TEM responses.

Table 3. Misfit details of four network models' predictions for the five-strata geoelectric model parameters.

	H_z		V_z		*rho*		Thickness (*h*)		*c*	
	MAPE	**RMSE**	**MAPE**	**RMSE**	**MAPE**	**RMSE**	**MAPE**	**RMSE**	**MAPE**	**RMSE**
GCN + LSTM	2.80	10.31	3.60	12.91	2.09	2.48	2.61	2.93	7.84	1.45
GCN	4.84	6.80	14.2	30.67	5.86	6.27	2.60	3.23	19.10	3.51
LSTM	7.23	28.1	5.833	12.94	4.90	5.84	5.54	6.44	25.32	4.29
MLP	19.86	72.9	21.72	60.44	8.17	9.01	6.55	8.15	20.54	3.90

4.2. Model 2

Model 2 is a nine-strata geoelectric model with a total of 17 predicted parameters. The reference comparative neural network models include MLP, LSTM, and traditional GCN. In the nine-strata geoelectric model (Figure 8a), the resistivity of each layer is, respectively, 50, 300, 100, 500, 200, 100, 300, 50, and 200 Ω·m. The thickness of the first four layers is 200, 250, 300, 500, 300, 100, 200, and 300 m. The bottom-most layer is considered to be an infinitely extending homogeneous space with infinite thickness. Layers 2, 4, 6, and 8 are complex resistivity layers exhibiting IP effects. The frequency correlation coefficients are 0.3, 0.4, 0.2, and 0.5, respectively.
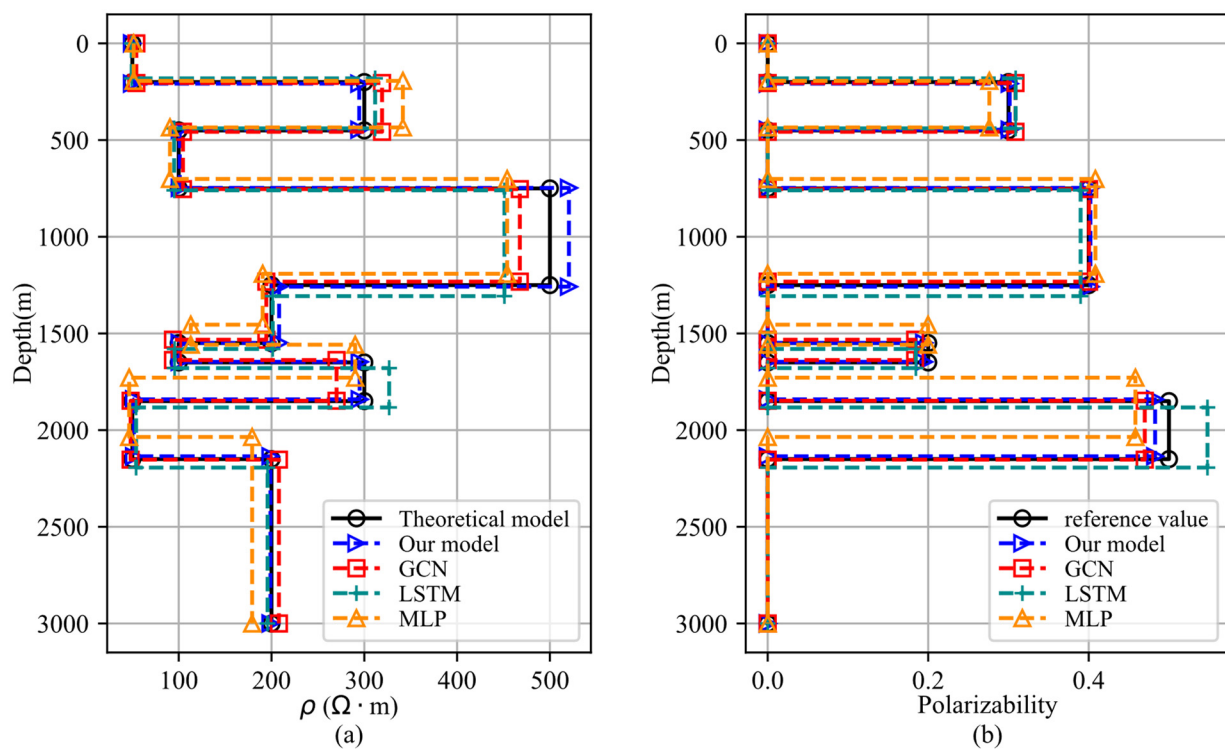

Figure 8. The predictions of different neural network models for the nine-strata geoelectric structure based on TEM responses. (**a**) represents the depth-resistivity relationship chart for the assumed and predicted nine-strata geoelectric structures. (**b**) represents the depth-IP (Induced Polarization) parameter relationship chart for the assumed and predicted nine-strata geoelectric structures.

From the predicted geoelectric structure (Figure 8a), it is observed that all four neural network models accurately predict the resistivity and thickness of the first, third, and fifth layers. However, for the second, fourth, seventh, and ninth layers, noticeable deviations are evident in the predicted resistivity results among different methods, with MLP exhibiting the largest deviation. For the resistivity of the fourth layer, except for the proposed method,

MLP, LSTM, and GCN all show significant discrepancies. Below the fifth layer, MLP's predicted results significantly deviate from the predefined geoelectric structure.

In the comparison of the accuracy in predicting the IP parameters (Figure 8b), it is observed that various methods achieve relatively accurate restoration of the IP parameters for the second and fourth layers. However, the accuracy decreases for predicting the IP parameters of the sixth and eighth layers. Similar to the resistivity-thickness relationship's prediction results (Figure 8a), below the fifth layer's structure, the predictive electric parameters of the traditional MLP model significantly deviate from the predefined geoelectric structure. Additionally, although LSTM's prediction accuracy is higher than that of MLP, it still exhibits a noticeable misfit. The two types of GCN models exhibit the highest accuracy in predicting the IP parameters. Detailed information about the predictions of the 9-strata electric structure parameters by the four network models is shown in Table 4.

Table 4. Comparative details of four network models' predictions for the nine-strata geoelectric model parameters.

	rho_1	rho_2	rho_3	rho_4	rho_5	rho_6	rho_7	rho_8	rho_9
Synthetic	50	300	100	500	200	100	300	50	200
GCN + LSTM	49.51	294.54	101.09	520.51	208.18	100.92	294.98	51.77	198.85
GCN	54.36	319.12	104.57	467.58	194.41	93.78	270.07	48.16	207.98
LSTM	49.32	311.66	95.14	450.98	201.29	95.59	326.77	54.06	195.71
MLP	51.42	341.59	90.57	453.96	190.50	112.99	290.16	46.60	179.12
	h_1	h_2	h_3	h_4	h_5	h_6	h_7	h_8	-
Synthetic	200	250	300	500	300	100	200	300	-
GCN + LSTM	208.09	238.33	300.97	510.82	290.38	98.37	193.75	294.66	-
GCN	205.01	252.15	296.34	478.74	300.10	105.23	210.50	304.56	-
LSTM	180.99	258.57	320.23	547.15	273.42	99.01	203.30	311.20	-
MLP	193.83	240.60	266.80	490.26	263.24	103.44	170.66	306.59	-
	c_1	c_2	c_3	c_4	c_5	c_6	c_7	c_8	c_9
Synthetic	-	0.3	-	0.4	-	0.2	-	0.5	-
GCN + LSTM	-	0.30	-	0.40	-	0.19	-	0.48	-
GCN	-	0.31	-	0.40	-	0.18	-	0.47	-
LSTM	-	0.31	-	0.39	-	0.18	-	0.55	-
MLP	-	0.28	-	0.41	-	0.20	-	0.46	-

Note: rho_i, h_i, c_i represent the resistivity, thickness, and Cole-Cole model frequency correction coefficient of the i-th layer, respectively.

Taking into account the comprehensive comparison of the misfits of various neural networks in predicting geoelectric model parameters (Figure 9a,b), their prediction accuracy from high to low ranks is as follows: our model, GCN, LSTM, and MLP. The intervals with larger error values are primarily concentrated in high-resistivity layers, particularly for layers with resistivity values of 500 $\Omega \cdot$m and 300 $\Omega \cdot$m. For layers with induced polarization effects, MLP's predictions show significant inaccuracies. LSTM starts exhibiting noticeable misfits from the fourth layer onwards.
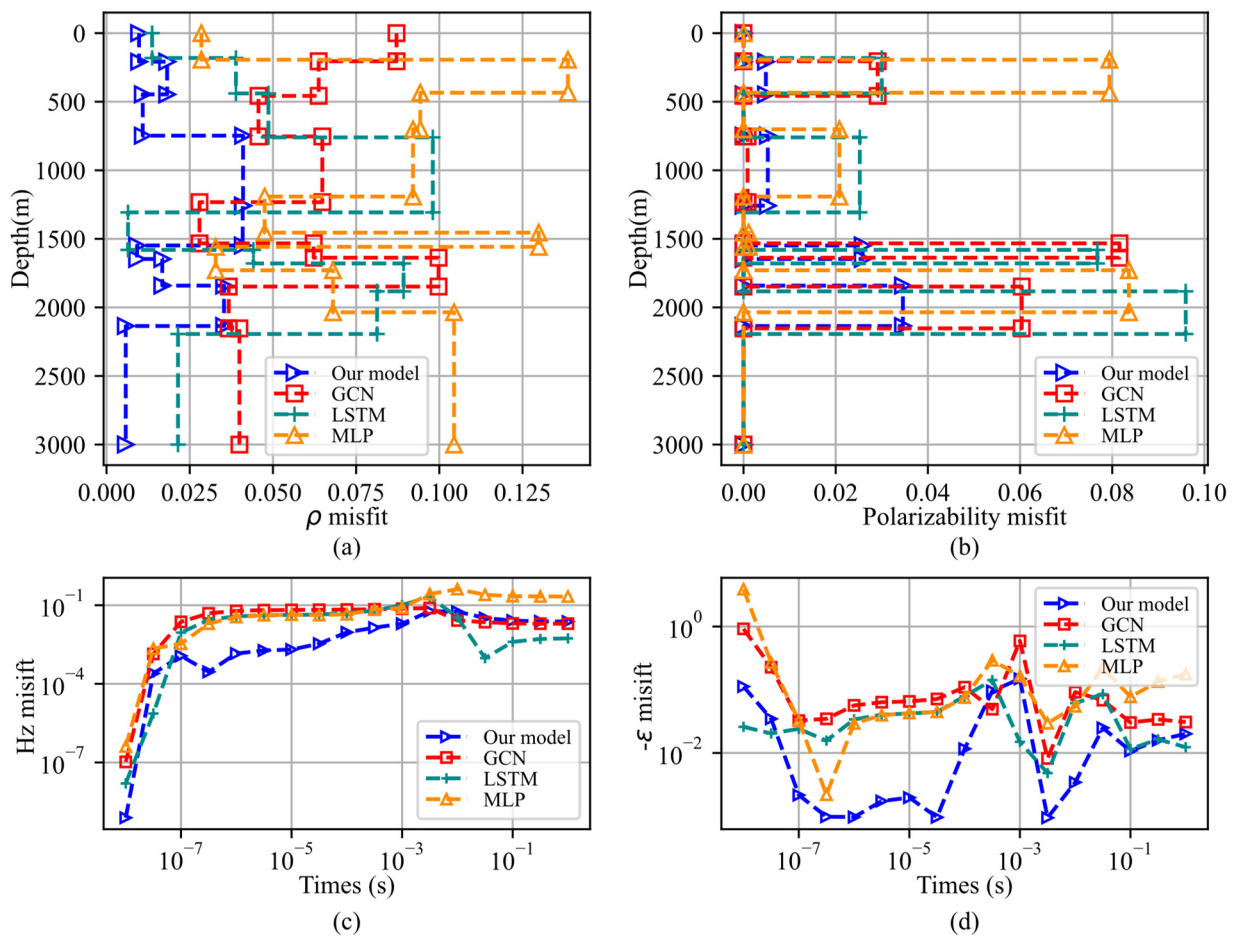
Figure 9. Misfit analysis of predicting the nine-strata geoelectric structure using different neural network models based on TEM responses. (**a**) Depth and resistivity misfits of the predicted nine-strata geoelectric structure, (**b**) Depth and IP parameter misfits of the predicted nine-layer geoelectric structure, (**c**) Induced magnetic field misfits in the predicted TEM responses, (**d**) Induced EMF misfits in the predicted TEM responses.

We conducted a comparative analysis of the accuracy of TME responses predicted using various neural network models (Figure 9c,d). The induction magnetic field misfit shows that within the observation time window range of 1×10^{-6} to 1×10^{-3} s, the predictive accuracy of our method is significantly superior to that of the network model by two orders of magnitude, reducing the fitting discrepancy from 1×10^{-2} to 1×10^{-4} (Figure 9c). This advantage is also reflected in the misfit of the induced EMF (Figure 9d). For the late-stage induced magnetic field after 1×10^{-3} s, GCN-based network models perform slightly worse than LSTM-based models. However, this performance difference is not observed in the misfit of the induced EMF. Using MAPE and RMSE metrics, we performed a comparative analysis of the errors in predicted geoelectric model parameters and the errors in corresponding induced TEM signals predicted using different network models (Table 5).

Table 5. Misfit details of four network models' predictions for the nine-strata geoelectric model parameters.

	H_z		V_z		*rho*		Thickness (*h*)		*c*	
	MAPE	**RMSE**	**MAPE**	**RMSE**	**MAPE**	**RMSE**	**MAPE**	**RMSE**	**MAPE**	**RMSE**
GCN + LSTM	1.13	1.66	1.78	3.61	1.56	1.86	2.12	2.33	0.89	1.41
GCN	9.40	11.04	10.40	14.50	4.53	5.17	6.53	7.19	2.35	3.81
LSTM	11.91	12.99	17.04	22.51	6.31	6.76	2.00	2.67	3.20	5.14
MLP	10.93	11.79	24.69	42.50	8.79	10.05	5.13	5.72	3.12	5.52

5. Discussion

5.1. Denoising

To assess the stability and generalization ability of the proposed neural network for inverting TEM data with consideration of IP effects, we designed a case study involving a noisy 5-layer geoelectric model. Gaussian random noise at levels of 5% and 10% was added to the TEM responses of a five-layer geoelectric model, with a noise-free case serving as the reference. The resistivity values for the five layers of the geoelectric model were set as follows: $\rho 1 = 300$ Ω·m, $\rho 2 = 200$ Ω·m, $\rho 3 = 500$ Ω·m, $\rho 4 = 50$ Ω·m and $\rho 5 = 1000$ Ω·m. The corresponding layer thicknesses were $h1 = 200$ m, $h2 = 300$ m, $h3 = 300$ m and $h4 = 300$ m. We considered a simple excitation polarization effect with variations only in the "m" coefficient, where the *m* values for the second and fourth layers were set to 0.3 and 0.4, respectively.

We compared the inversion performance of the proposed algorithm on noisy TEM data with noise levels of 5% and 10% (see Table 6). As the noise increased, both the MAPE and the RMSE gradually increased. To account for the noise levels, we subtracted the noise level from the MAPE, considering it as a relative MAPE error. The Re-MAPE increased continuously with the rising noise levels, indicating that as the noise grew, the neural network's generalization ability decreased, rising from an initial 4.04% to 7.68%.

Table 6. Inversion accuracy with noise data.

HKH-Type Model	RMSE (%)	MAE (%)	Re-MAE
no noise	14.07	4.04	4.04
5% noise	20.31	9.91	4.91
10% noise	31.59	17.68	7.68

Furthermore, the RMSE reflected the level of data consistency, with larger RMSE values indicating poorer data consistency. This suggests that as noise levels increased, the stability of the neural network also decreased.

Figure 10 presents the inversion-predicted geoelectric structure and the alignment status of time-domain-induced signals generated using the five-layer model at different noise levels. For noise-free data, the proposed algorithm achieves precise reconstruction of resistivity, thickness, and induced polarization parameters for the assumed geoelectric model, resulting in a MAPE of 4.04%. For data with 5% and 10% random noise, the resistivity, thickness, and polarization parameters can still broadly characterize the underlying trends, but the precision in capturing details has diminished. Particularly, at a noise level of 10%, the depth estimation for the third layer appears shallower.
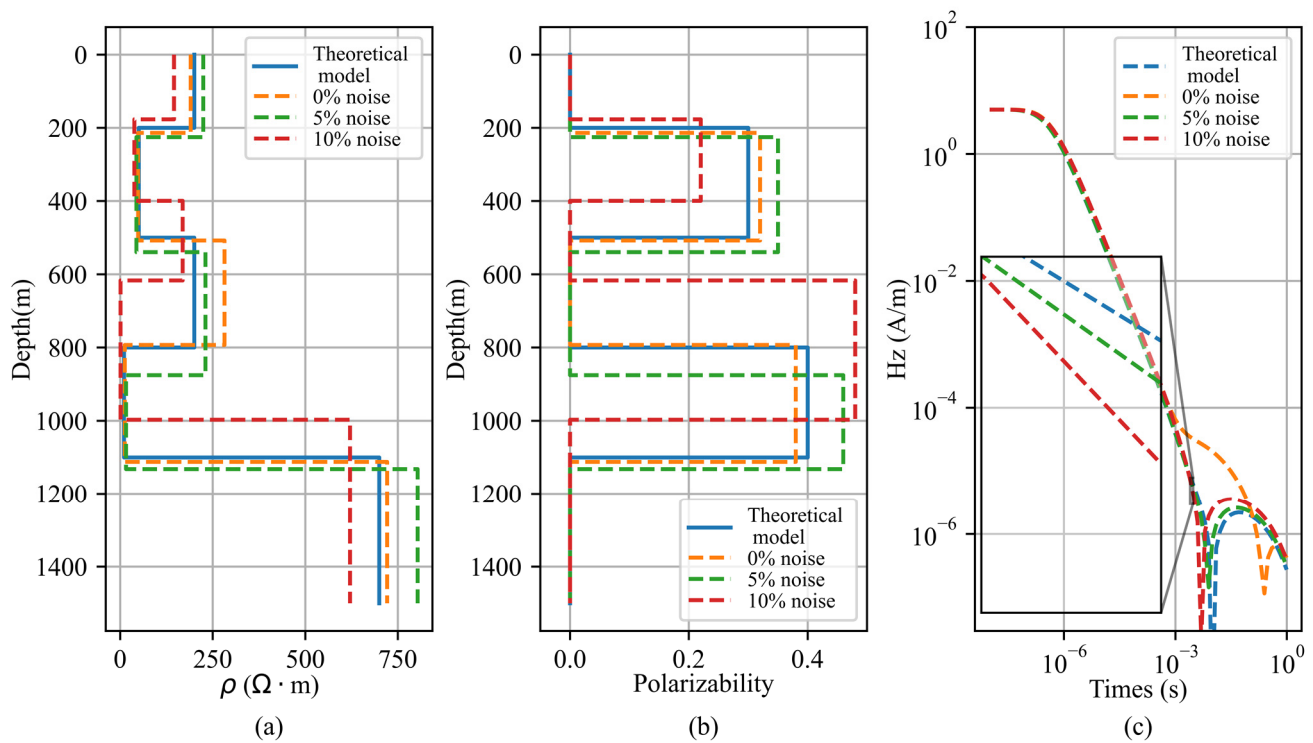
Figure 10. Inversion outcomes of the five-strata geoelectric model with an intermediate polarization layer. (**a**) represent the theoretical geoelectric model and inversed geoelectric model; (**b**) represent the predictive polarization parameters and the theoretical parameters; (**c**) represent the HZ data fitting curve.

5.2. Complex Model

To further validate the network's capability to handle complex geoelectric structures, a 3D simulation model of a seafloor massive sulfide (SMS) deposit has been established. The resistivity of the overlying layer of minerals is set to 10 Ω·m. As magmatic-hydrothermal upwelling occurs, alteration zones gradually form around the upwelling channels, resulting in electrical resistivities of 0.5, 1, and 2 Ω·m, corresponding to strong, medium, and weak alteration regions, respectively. In the intermediate region between two magmatic-hydrothermal upwelling channels, there exists an alteration zone (depicted in yellow) that does not make direct contact with the seafloor surface alongside a buried, intact sulfide sedimentary mineral deposit (depicted in black). Figure 11 displays a perspective view, top view, and sliced view of this 3D model.

The inversion results of the proposed method are compared with those of the traditional gradient inversion method, as illustrated in Figure 12. The traditional gradient inversion method employs OCCAM inversion [51], and the specific implementation and inversion termination strategy are referenced from the literature. Due to the absence of a strategy for optimizing polarization parameters, the inversion results at y = 70 m and y = 110 m in the gradient inversion show an inability to accurately recover the predefined geoelectric structure of SMS. In contrast, the inversion slices obtained using the proposed method demonstrate an effective characterization of the fundamental geoelectric structural features of magmatic-hydrothermal upwelling channels, alteration regions, and buried SMS minerals. This underscores that the TEM inversion framework based on the GCN-LSTM neural network can effectively account for the induced polarization effect in electrical media while achieving accurate geoelectric structure reconstructions.
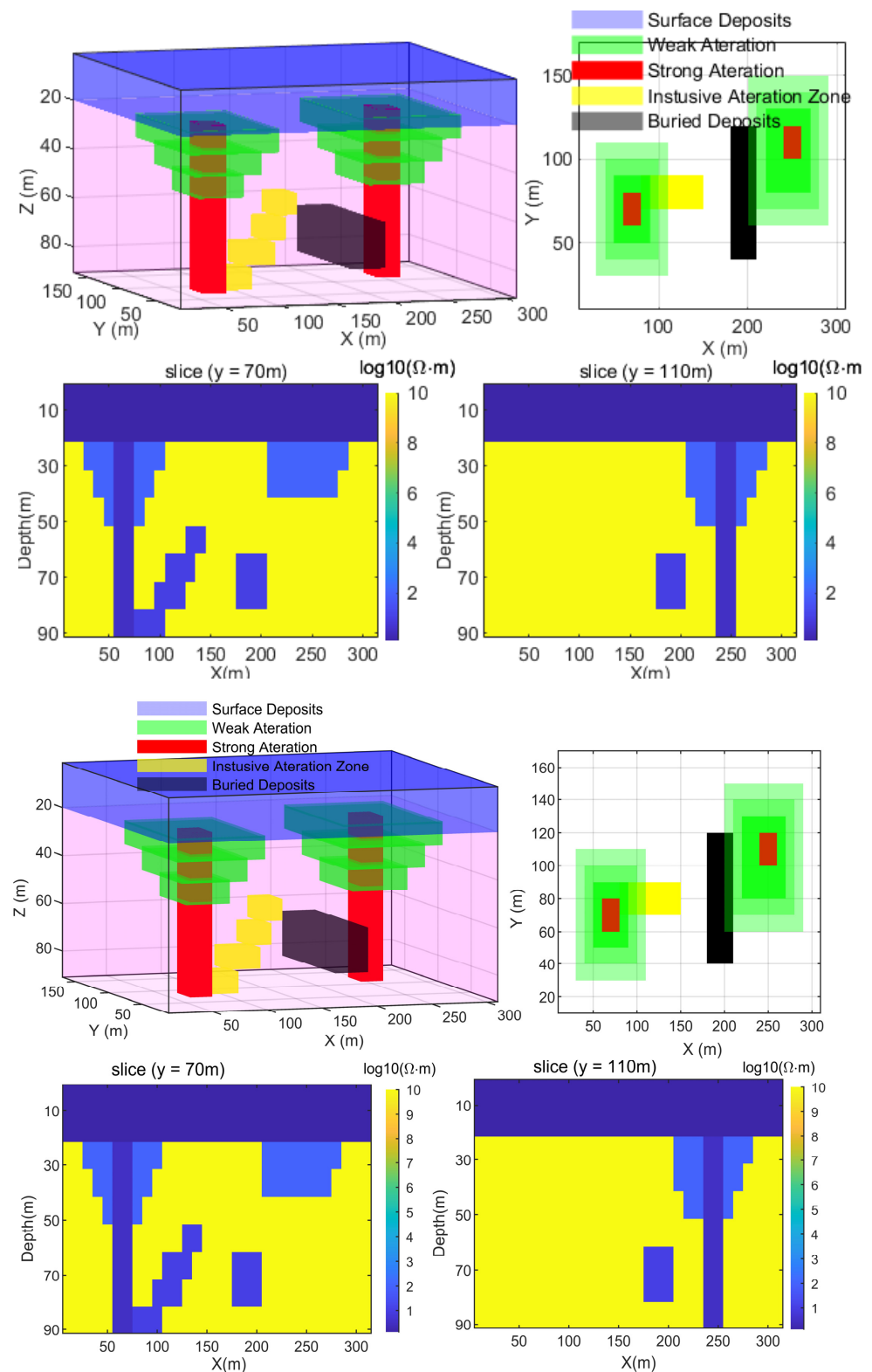
Figure 11. A 3D simulation model of a seafloor massive sulfide (SMS) deposit is depicted here. With the upwelling of magmatic-hydrothermal fluids (in red), gradual alteration of the surrounding rock layers occurs, resulting in the formation of alteration zones. These alteration zones, progressing from the inner to outer regions, exhibit varying degrees of alteration—strong, moderate, and weak (in green). In the intermediate space between two magmatic-hydrothermal upwelling channels, there is an alteration zone (in yellow) that does not make direct contact with the seafloor surface, along with a buried intact sulfide sedimentary mineral deposit (in black).
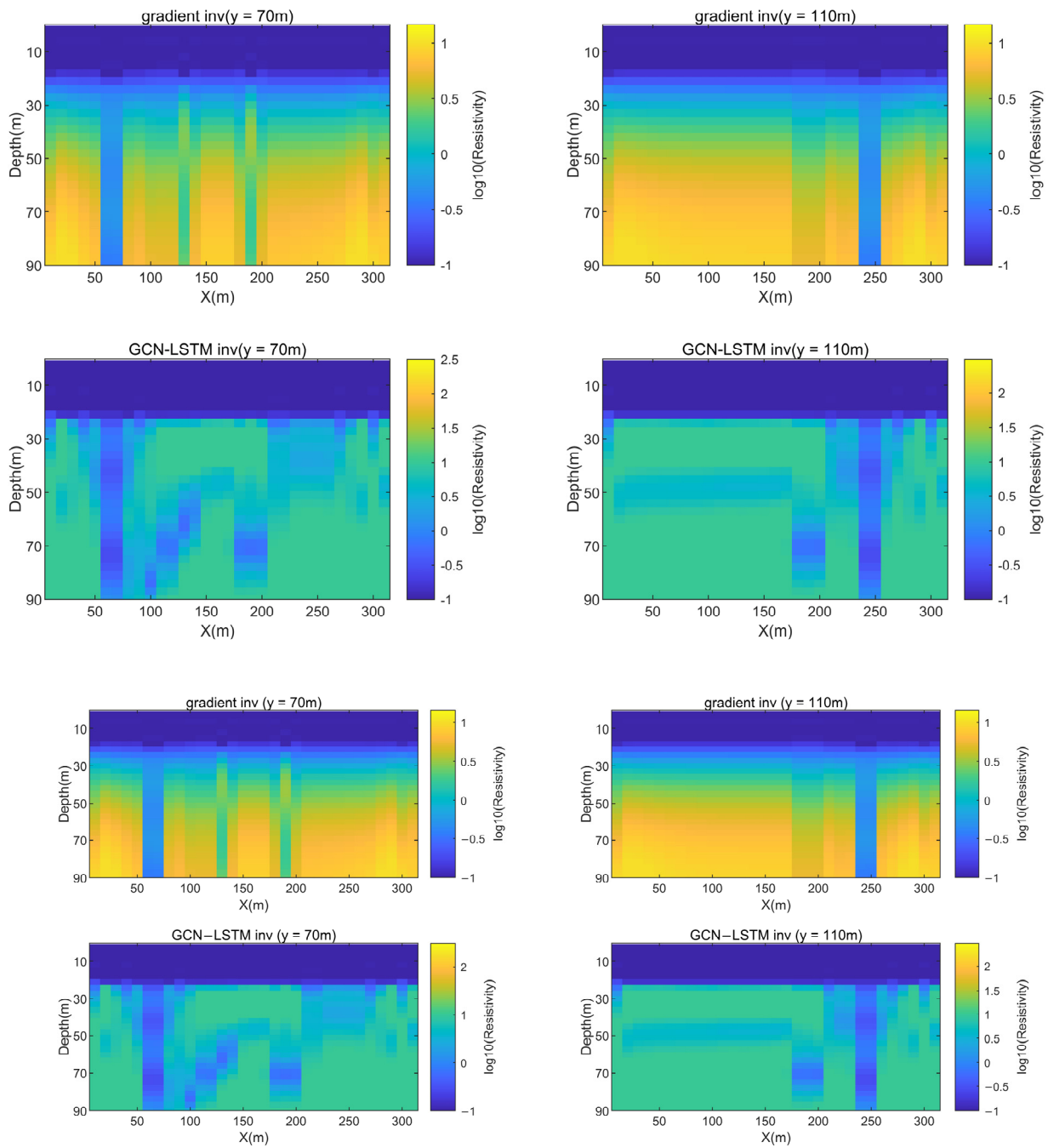
Figure 12. Comparison between the gradient inversion and the SMS model of the proposed GCN-LSTM networks inversion.

6. Conclusions

A strata electrical imaging neural network model based on graph topology is established. This model utilizes GCN to capture non-Euclidean features, such as resistivity-thickness relationships and employs LSTM to capture long-range dependency features. The weakness of GCN in capturing distant node relationships is compensated for by LSTM. The effectiveness of the approach was validated using case studies involving five-strata and nine-strata geoelectric models. Comparative disintegration experiments included results contrasting with traditional MLP, LSTM, and GCN, further illustrating the robustness of the proposed network model. Misfit analysis indicates that, compared to the traditional MLP, the proposed method reduces prediction errors in electrical structure estimation from 10–20% down to 2–3%.

References

1. Wu, S.; Huang, Q.; Zhao, L. A Deep Learning-Based Network for the Simulation of Airborne Electromagnetic Responses. *Geophys. J. Int.* **2022**, *233*, 253–263. [CrossRef]
2. Wang, S.; Yu, Y.; Zhao, X.; Wang, Y.; Gao, Q.; Ji, Y. Characterization of Excitation Effects and Data Interpretation of Combined Time-Domain Multiwaveform Transmission Currents. *IEEE Sens. J.* **2023**, *23*, 17159–17172. [CrossRef]
3. Li, J.; Farquharson, C.G.; Hu, X. Three Effective Inverse Laplace Transform Algorithms for Computing Time-Domain Electromagnetic responsesInverse Laplace Transform Algorithms. *Geophysics* **2016**, *81*, E113–E128. [CrossRef]
4. Cai, H.; Liu, M.; Zhou, J.; Li, J.; Hu, X. Effective 3D-Transient Electromagnetic Inversion Using Finite-Element Method with a Parallel Direct Solver. *Geophysics* **2022**, *87*, E377–E392. [CrossRef]
5. Cai, H.; Hu, X.; Xiong, B.; Zhdanov, M.S. Finite-Element Time-Domain Modeling of Electromagnetic Data in General Dispersive Medium Using Adaptive Padé Series. *Comput. Geosci.* **2017**, *109*, 194–205. [CrossRef]
6. Maurya, P.K.; Christensen, F.E.; Kass, M.A.; Pedersen, J.B.; Frederiksen, R.R.; Foged, N.; Christiansen, A.V.; Auken, E. Technical Note: Efficient Imaging of Hydrological Units below Lakes and Fjords with a Floating, Transient Electromagnetic (FloaTEM) System. *Hydrol. Earth Syst. Sci.* **2022**, *26*, 2813–2827. [CrossRef]
7. Sandersen, P.B.E.; Kallesøe, A.J.; Møller, I.; Høyer, A.-S.; Jørgensen, F.; Pedersen, J.B.; Christiansen, A.V. Utilizing the Towed Transient ElectroMagnetic Method (tTEM) for Achieving Unprecedented near-Surface Detail in Geological Mapping. *Eng. Geol.* **2021**, *288*, 106125. [CrossRef]
8. Li, R.; Hu, X.; Xu, D.; Liu, Y.; Yu, N. Characterizing the 3D Hydrogeological Structure of a Debris Landslide Using the Transient Electromagnetic Method. *J. Appl. Geophys.* **2020**, *175*, 103991. [CrossRef]
9. Pondthai, P.; Everett, M.E.; Micallef, A.; Weymer, B.A.; Faghih, Z.; Haroon, A.; Jegen, M. 3D Characterization of a Coastal Freshwater Aquifer in SE Malta (Mediterranean Sea) by Time-Domain Electromagnetics. *Water* **2020**, *12*, 1566. [CrossRef]
10. Auken, E.; Foged, N.; Larsen, J.J.; Lassen, K.V.T.; Maurya, P.K.; Dath, S.M.; Eiskjær, T.T. tTEM—A Towed Transient Electromagnetic System for Detailed 3D Imaging of the Top 70 m of the Subsurface. *Geophysics* **2019**, *84*, E13–E22. [CrossRef]
11. Cheng, M.; Yang, D.; Luo, Q. Interpreting Surface Large-Loop Time-Domain Electromagnetic Data for Deep Mineral Exploration Using 3D Forward Modeling and Inversion. *Minerals* **2023**, *13*, 34. [CrossRef]
12. Grombacher, D.; Maurya, P.K.; Lind, J.C.; Lane, J.; Auken, E. Rapid Mapping of Hydrological Systems in Tanzania Using a Towed Transient Electromagnetic System. *Groundwater* **2022**, *60*, 35–46. [CrossRef]
13. Lin, J.; Chen, J.; Liu, F.; Zhang, Y. The Helicopter Time-Domain Electromagnetic Technology Advances in China. *Surv. Geophys.* **2021**, *42*, 585–624. [CrossRef]
14. Maurya, P.K.; Christiansen, A.V.; Pedersen, J.; Auken, E. High Resolution 3D Subsurface Mapping Using a Towed Transient Electromagnetic System - tTEM: Case Studies. *Near Surf. Geophys.* **2020**, *18*, 249–259. [CrossRef]
15. Li, R.; Hu, X.; Li, J. Pseudo-3D Constrained Inversion of Transient Electromagnetic Data for a Polarizable SMS Hydrothermal System in the Deep Sea. *Stud. Geophys. Et Geod.* **2018**, *62*, 512–533. [CrossRef]
16. Yang, H.; Cai, H.; Liu, M.; Xiong, Y.; Long, Z.; Li, J.; Hu, X. Three-dimensional Inversion of Semi-airborne Transient Electromagnetic Data Based on Finite Element Method. *Near Surf. Geophys.* **2022**, *20*, 661–678. [CrossRef]
17. Wu, Q.; Ma, Y.; Li, D.; Wang, Y.; Ji, Y. Denoising Algorithm of Ground-Airborne Time-Domain Electromagnetic Method Based on Variational Bayesian-Based Adaptive Kalman Filter (VBAKF). *J. Appl. Geophys.* **2022**, *202*, 104674. [CrossRef]
18. Barsukov, P.O.; Fainberg, E.B. Mapping Bedrock Topography and Moraine Deposits by Transient Electromagnetic Sounding: Oslo Graben, Norway. *Near Surf. Geophys.* **2020**, *18*, 123–133. [CrossRef]
19. Bai, P.; Vignoli, G.; Hansen, T.M. 1D Stochastic Inversion of Airborne Time-Domain Electromagnetic Data with Realistic Prior and Accounting for the Forward Modeling Error. *Remote Sens.* **2021**, *13*, 3881. [CrossRef]
20. Kong, R.; Hu, X.; Cai, H. Three-dimensional joint inversion of gravity and magnetic data using Gramian constraints and Gauss-Newton method. *Chin. J. Geophys.* **2023**, *66*, 3493–3513.
21. Wang, X.; Cai, H.; Liu, L.; Revil, A.; Hu, X. Three-Dimensional Inversion of Long-Offset Transient Electromagnetic Method over Topography. *Minerals* **2023**, *13*, 908. [CrossRef]
22. Belliveau, P.; Haber, E. Achieving Depth Resolution with Gradient Array Survey Data through Transient Electromagnetic Inversion. In Proceedings of the SEG International Exposition and Annual Meeting, Dallas, TX, USA, 16–21 October 2016; pp. 857–861. [CrossRef]

23. Murzina, E.V.; Pospeev, A.V.; Seminskiy, I.K.; Buddo, I.V.; Nemtseva, D.B.; Emelianov, V.S.; Agafonov, Y.A. Features of High-Density Transient Electromagnetic Sounding Data Inversion under Oil and Gas Prospecting in the Nepa-Botuoba Anteclise Area. *Jour* **2022**, *45*, 137–151. [CrossRef]

24. Li, R.; Zhuang, Q.; Yu, N.; Li, R.; Zhang, H. Improved Hybrid Particle Swarm Optimizer with Sine-Cosine Acceleration Coefficients for Transient Electromagnetic Inversion. *Curr. Bioinform.* **2021**, *16*, 60–76. [CrossRef]

25. Li, R.; Yu, N.; Wang, X.; Liu, Y.; Cai, Z.; Wang, E. Model-Based Synthetic Geoelectric Sampling for Magnetotelluric Inversion with Deep Neural Networks. *IEEE Trans. Geosci. Remote Sens.* **2020**, *60*, 1–14. [CrossRef]

26. Asif, M.R.; Bording, T.S.; Maurya, P.K.; Zhang, B.; Fiandaca, G.; Grombacher, D.J.; Christiansen, A.V.; Auken, E.; Larsen, J.J. A Neural Network-Based Hybrid Framework for Least-Squares Inversion of Transient Electromagnetic Data. *IEEE Trans. Geosci. Remote Sens.* **2022**, *60*, 1–10. [CrossRef]

27. Li, R.; Wu, X.; Tian, H.; Yu, N.; Wang, C. Hybrid Memetic Pretrained Factor Analysis-Based Deep Belief Networks for Transient Electromagnetic Inversion. *IEEE Trans. Geosci. Remote Sens.* **2022**, *60*, 1–20. [CrossRef]

28. Kozhevnikov, N.O.; Antonov, E.Y. Aftereffects in the Transient Electromagnetic Method: Inductively Induced Polarization. *Russ. Geol. Geophys.* **2021**, *62*, 1440–1448. [CrossRef]

29. Grombacher, D.; Auken, E.; Foged, N.; Bording, T.; Foley, N.; Doran, P.T.; Mikucki, J.; Dugan, H.A.; Garza-Giron, R.; Myers, K.; et al. Induced Polarization Effects in Airborne Transient Electromagnetic Data Collected in the McMurdo Dry Valleys, Antarctica. *Geophys. J. Int.* **2021**, *226*, 1574–1583. [CrossRef]

30. Wu, C.; Zou, C.; Wu, T.; Shen, L.; Zhou, J.; Tao, C. Experimental Study on the Detection of Metal Sulfide under Seafloor Environment Using Time Domain Induced Polarization. *Mar. Geophys. Res.* **2021**, *42*, 17. [CrossRef]

31. Liu, H.; Zhao, X.; Yu, Y.; Qiu, S.; Ji, Y. 3-D Full-Waveform Modeling and Analysis of Induced Polarization and Magnetic Viscosity Effect in Time-Domain Electromagnetic Method. *IEEE Trans. Geosci. Remote Sens.* **2023**, *61*, 1–14. [CrossRef]

32. He, Z.; Cai, H.; Li, S.; Xian, J.; Hu, X. Extracting IP Parameters of Rock Samples Using Machine Learning. *Geophys. J. Int.* **2023**, *235*, 862–878. [CrossRef]

33. Ageev, V.V. On the Nature of Negative Values of Induced Polarization in the Transient Electromagnetic Process When Working with an Axial Electrical Installation on the Sea Shelf. *Izv. Phys. Solid Earth* **2023**, *59*, 328–336. [CrossRef]

34. Aigner, L.; Katona, T.; Michel, H.; Ahmed, A.; Hermans, T.; Flores Orozco, A. Quantification of Clay Content Using the Transient Electromagnetic and Spectral Induced Polarization Method. In Proceedings of the EGU General Assembly 2021, Online, 19–30 April 2021.

35. Fedeli, A.; Schenone, V.; Pastorino, M.; Randazzo, A. An LSTM Based Strategy for Data and Model Calibration in Subsurface Electromagnetic Imaging. In Proceedings of the 2022 IEEE Conference on Antenna Measurements and Applications (CAMA), Guangzhou, China, 14–17 December 2022; pp. 1–3.

36. Wu, F.; Fan, M.; Liu, W.; Liang, B.; Zhou, Y. An Efficient Time-Domain Electromagnetic Algorithm Based on LSTM Neural Network. *IEEE Antennas Wirel. Propag. Lett.* **2021**, *20*, 1322–1326. [CrossRef]

37. Guo, L.; Song, G.; Wu, H. Complex-Valued Pix2pix—Deep Neural Network for Nonlinear Electromagnetic Inverse Scattering. *Electronics* **2021**, *10*, 752. [CrossRef]

38. Hu, K.; Wu, J.; Li, Y.; Lu, M.; Weng, L.; Xia, M. FedGCN: Federated Learning-Based Graph Convolutional Networks for Non-Euclidean Spatial Data. *Mathematics* **2022**, *10*, 1000. [CrossRef]

39. Wu, Q.; Zhao, W.; Li, Z.; Wipf, D.P.; Yan, J. NodeFormer: A Scalable Graph Structure Learning Transformer for Node Classification. *Adv. Neural Inf. Process. Syst.* **2022**, *35*, 27387–27401.

40. Chen, D.; Lin, Y.; Zhao, G.; Ren, X.; Li, P.; Zhou, J.; Sun, X. Topology-Imbalance Learning for Semi-Supervised Node Classification. In Proceedings of the Advances in Neural Information Processing Systems, Online, 6–14 December 2021; Curran Associates, Inc.: Red Hook, NY, USA, 2021; Volume 34, pp. 29885–29897.

41. Chen, Y.; Coskunuzer, B.; Gel, Y. Topological Relational Learning on Graphs. In Proceedings of the Advances in Neural Information Processing Systems, Online, 6–14 December 2021; Curran Associates, Inc.: Red Hook, NY, USA, 2021; Volume 34, pp. 27029–27042.

42. Chen, J.; He, H.; Wu, F.; Wang, J. Topology-Aware Correlations Between Relations for Inductive Link Prediction in Knowledge Graphs. In Proceedings of the AAAI Conference on Artificial Intelligence, Vancouver, BC, Canada, 2–9 February 2021; Volume 35, pp. 6271–6278. [CrossRef]

43. Behera, R.K.; Jena, M.; Rath, S.K.; Misra, S. Co-LSTM: Convolutional LSTM Model for Sentiment Analysis in Social Big Data. *Inf. Process. Manag.* **2021**, *58*, 102435. [CrossRef]

44. Bi, J.; Zhang, X.; Yuan, H.; Zhang, J.; Zhou, M. A Hybrid Prediction Method for Realistic Network Traffic with Temporal Convolutional Network and LSTM. *IEEE Trans. Autom. Sci. Eng.* **2022**, *19*, 1869–1879. [CrossRef]

45. Li, J.; Wang, X.; Hu, X.; Yuan, W.; Wang, P. Land-Based TEM Data Processing: From Turn-off Ramp to Full Waveform. *Geophysics*, 2022; *Preprints*.

46. Li, R.; Gao, L.; Yu, N.; Li, J.; Liu, Y.; Wang, E.; Feng, X. Memetic Strategy of Particle Swarm Optimization for One-Dimensional Magnetotelluric Inversions. *Mathematics* **2021**, *9*, 519. [CrossRef]

47. Nabighian, M.; projecteditor; Corbett, J. *Electromagnetic Methods in Applied Geophysics*; Society of Exploration Geophysicists: Houston, TX, USA, 1988.

48. Wei, W.; Cai, J.; Hu, X.; Han, Q. An Electrical Conductivity Model for Fractal Porous Media: Fractal and Electrical Conductivity. *Geophys. Res. Lett.* **2015**, *42*, 4833–4840. [CrossRef]
49. Madsen, L.M.; Fiandaca, G.; Auken, E.; Christiansen, A.V. Time-Domain Induced Polarization—An Analysis of Cole–Cole Parameter Resolution and Correlation Using Markov Chain Monte Carlo Inversion. *Geophys. J. Int.* **2017**, *211*, 1341–1353. [CrossRef]
50. Li, R.; Zhang, H.; Zhuang, Q.; Li, R.; Chen, Y. BP Neural Network and Improved Differential Evolution for Transient Electromagnetic Inversion. *Comput. Geosci.* **2020**, *137*, 104434. [CrossRef]
51. Li, R.; Yu, N.; Wang, E.; Wang, X.; Mao, L.; Sun, Z.; Wu, X. Airborne Transient Electromagnetic Simulation: Detecting Geoelectric Structures for HVdc Monopole Operation. *IEEE Geosci. Remote Sens. Mag.* **2021**, *10*, 274–288. [CrossRef]
52. Shi, X.; Chen, Z.; Wang, H.; Yeung, D.; Wong, W.; Woo, W. Convolutional LSTM Network: A Machine Learning Approach for Precipitation Nowcasting. In *Advances in Neural Information Processing Systems*; The MIT Press: Cambridge, MA, USA, 13 June 2015.
53. Greff, K.; Srivastava, R.K.; Koutnik, J.; Steunebrink, B.R.; Schmidhuber, J. LSTM: A Search Space Odyssey. *IEEE Trans. Neural Netw. Learn. Syst.* **2017**, *28*, 2222–2232. [CrossRef]
54. Sherstinsky, A. Fundamentals of Recurrent Neural Network (RNN) and Long Short-Term Memory (LSTM) Network. *Phys. D Nonlinear Phenom.* **2020**, *404*, 132306. [CrossRef]
55. Gers, F.A.; Schmidhuber, J.; Cummins, F. Learning to Forget: Continual Prediction with LSTM. *Neural Comput.* **2000**, *12*, 2451–2471. [CrossRef]
56. Deepa, N.; Prabakeran, S.; Devi, T. (NMRNN-LSTM)—Novel Modified RNN with Long and Short-Term Memory Unit in Healthcare and Big Data Applications. In Proceedings of the 2022 International Conference on Advancements in Smart, Secure and Intelligent Computing (ASSIC), Bhubaneswar, India, 19–20 November 2022; pp. 1–6. [CrossRef]
57. Zhao, L.; Song, Y.; Zhang, C.; Liu, Y.; Wang, P.; Lin, T.; Deng, M.; Li, H. T-GCN: A Temporal Graph Convolutional Network for Traffic Prediction. *IEEE Trans. Intell. Transp. Syst.* **2020**, *21*, 3848–3858. [CrossRef]
58. Hu, J.; Li, X.; Coleman, K.; Schroeder, A.; Ma, N.; Irwin, D.J.; Lee, E.B.; Shinohara, R.T.; Li, M. SpaGCN: Integrating Gene Expression, Spatial Location and Histology to Identify Spatial Domains and Spatially Variable Genes by Graph Convolutional Network. *Nat. Methods* **2021**, *18*, 1342–1351. [CrossRef] [PubMed]
59. He, X.; Deng, K.; Wang, X.; Li, Y.; Zhang, Y.; Wang, M. LightGCN: Simplifying and Powering Graph Convolution Network for Recommendation. In Proceedings of the 43rd International ACM SIGIR Conference on Research and Development in Information Retrieval, Virtual, 25–30 July 2020; pp. 639–648. [CrossRef]
60. Li, G.; Knoop, V.L.; Van Lint, H. Multistep Traffic Forecasting by Dynamic Graph Convolution: Interpretations of Real-Time Spatial Correlations. *Transp. Res. Part C: Emerg. Technol.* **2021**, *128*, 103185. [CrossRef]
61. Cui, Z.; Henrickson, K.; Ke, R.; Wang, Y. Traffic Graph Convolutional Recurrent Neural Network: A Deep Learning Framework for Network-Scale Traffic Learning and Forecasting. *IEEE Trans. Intell. Transport. Syst.* **2020**, *21*, 4883–4894. [CrossRef]